Analytical Study of Land Surface Temperature and Land Cover Indices in Major Australian Cities: Implications for Urban Planning and Mitigating Urban Heat Islands

1. Introduction

As urban populations continue to grow, more individuals are confronted with an escalating threat of urban heat islands (UHI), a heat accumulation phenomenon caused by urban development and industrialization (Rizwan et al., 2008; Yang et al., 2016). UHI can lead to thermal discomfort, especially in densely populated urban zones, where these effects are most pronounced (Nuruzzaman, 2015; Yin et al., 2023). Moreover, UHI can significantly increase the energy consumption needed to cool buildings by as much as 20%, resulting in a surge in energy demand (Li et al., 2019). The health consequences of UHI are particularly devastating in the summer, placing vulnerable groups such as children and the elderly at risk of heat-related stresses, and in severe cases, even fatality (Parker, 2010). UHI impacts are being exacerbated by climate change, which is expected to cause more frequent and severe heat waves (Alexander, 2020; Sharma et al., 2019). This emphasizes the imperative for proactive interventions to mitigate the detrimental effects of UHI on public well-being.

Transformation of land cover due to urbanization has profound effects on the urban land surface temperature (LST) (Shahfahad et al., 2022). For example, the urban canopy of multilayered buildings efficiently traps heat and obstructs wind flow, reducing heat dissipation by convection (Nuruzzaman, 2015). Increase in impermeable surfaces, such as asphalt and concrete, leads to rapid stormwater run-off, decreasing the cooling effect of surface evaporation (Mohajerani et al., 2017). The removal of vegetation cover substantially contributes to the elevated LST by reducing shading effects and cooling benefits of evapotranspiration (Santamouris, 2015). Water bodies exhibit lower temperatures due to their high specific heat capacity, which causes them to heat up more slowly (Gunawardena et al., 2017). As a result of air convection, water bodies can cool temperatures of land surface area within 1 kilometre, highlighting the cooling effects of urban water bodies, such as wetlands (Murakawa et al., 1991; R. Sun et al., 2012). Quantitative analyses of the relationship between land cover and urban temperatures can empower urban planners to pinpoint the underlying factors of UHI and develop innovative, localized strategies for mitigating UHI.

Remote sensing technology and geographic information systems (GIS) have been used to examine the impact of land cover changes on urban LST in several studies. Land cover indices can be calculated from multispectral satellite imagery to estimate the proportion of different land cover in each pixel. For example, Q. Sun et al. (2012) used spectral indices, such as Normalized Difference Vegetation Index (NDVI) and Normalized Difference Built-up Index (NDBI) to study the effects of land cover on LST of Guangzhou, China. Similarly, Alexander (2020) calculated the normalized difference spectral indices using all combinations of the first seven bands of Landsat 8 satellite imagery to understand spatial patterns of LST in Aarhus, Denmark. Land cover indices can also be used in a time-series analysis, as exemplified by Ahmed et al. (2013), who used NDVI, NDBI, Normalized Difference Water Index (NDWI), and Normalized Difference Bareness Index (NDBaI) to assess the impact of land cover changes over time on LST in Dhaka, Bangladesh. These studies show that spectral indices can be used as valuable proxies for land cover attributes, which help us understand the complex interplay between land cover and LST in urban environments.

Australian cities are subjected to UHI effects of significant magnitude, as well as extreme heat events that last multiple days (Rogers et al., 2019; Santamouris, 2015). According to projections from the Australian Bureau of Statistics (2014), the percentage of Australians residing in capital cities is anticipated to rise from 66% in 2013 to 72% by 2053. The combined risk of projected growth of Australia's urban population and the heightened occurrence and severity of heatwaves could lead to an increase in heat-related morbidity and mortality in Australian cities. This study aims to use remote sensing and GIS to examine the relationship between land cover and LST across four major Australian cities, namely Adelaide, Melbourne, Sydney, and Brisbane. The study used similar statistical approaches to previous studies mentioned like correlation analysis; however, there were some major modifications. Firstly, instead of using widely used indices like NDVI, the study utilizes more sophisticated spectral indices, including Enhanced Vegetation Index (EVI), Built-up Index (BU), and Modified Normalized Difference Water Index (MNDWI) as proxies for vegetated, built-up, and water land cover classes, respectively. Secondly, the study focuses on smaller fully urban areas, specifically a Statistical Area Level 4 (SA4) of each city, rather than the whole capital city, so that any variation in LST observed would be due to differences in urban land cover.

2. Materials and Methods

2.1 Study Area and Datasets

Four SA4s were selected as study areas from each capital city based on the location of the central business district, as outlined in *Table 1*. The spatial context of each study area is illustrated in *Figure 1*. For simplicity, each SA4 will be referenced in this paper by the capital city it is situated.

Table 1: The SA4s (study area) and the state and greater capital city at which each study area is situated

State	Greater Capital City	SA4 (Study area)
Victoria	Melbourne	Melbourne – Inner
New South Wales	Sydney	Sydney – City and Inner South
Queensland	Brisbane	Brisbane – Inner City
South Australia	Adelaide	Adelaide – West

Figure 1: Location of each SA4 of focus relative to its greater capital city and state

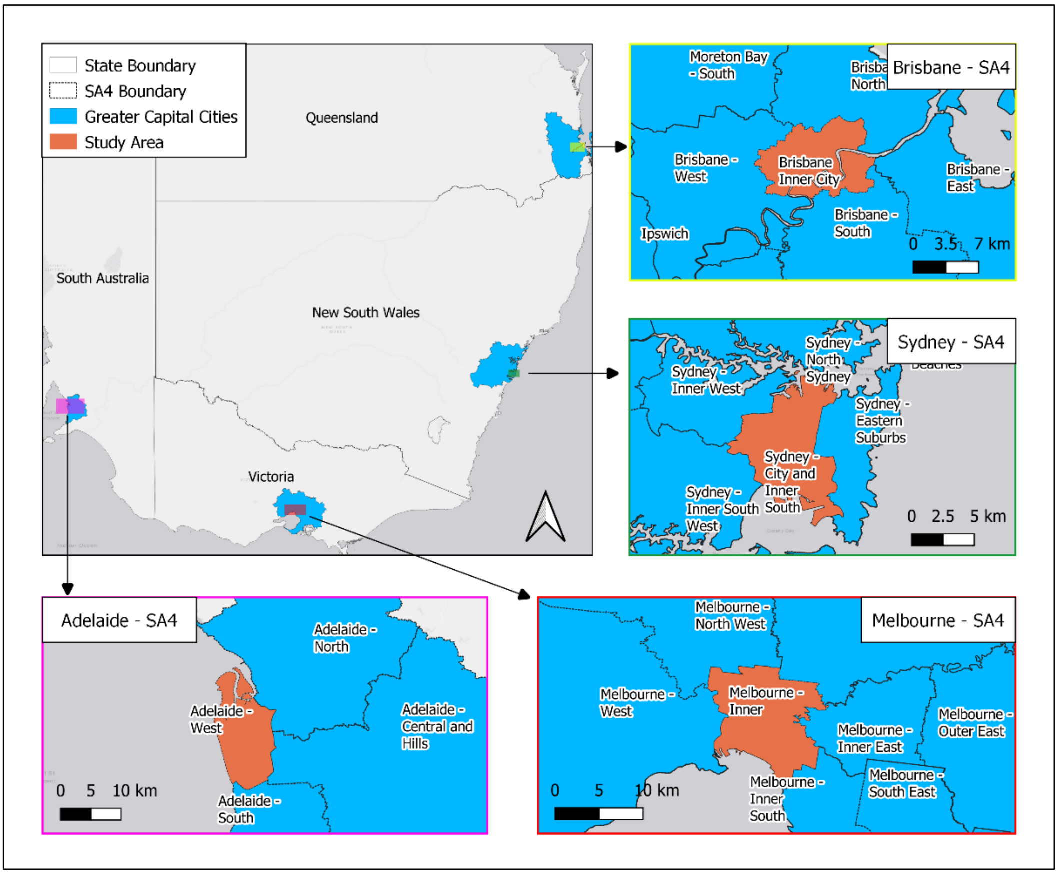

Source: Digital boundary files from Australian Bureau of Statistics (ABS), 2021

All of the study areas had high population density levels, with Sydney ranking the highest and Adelaide the lowest (*Table 2*). However, Adelaide had the highest demographic composition of residents aged below 10 and above 60 years (*Table 2*), both of which are highly susceptible to extreme heat and UHI effects.

Table 2: Background statistics of the study areas in 2021

SA4 (Study area)	Population	Area (ha)	Population density (persons/km^2)	Population under 10 years old (%)	Population above 60 years old (%)
Melbourne – Inner	627,671	14,245.8	4,406	7.6	16
Sydney – City and Inner South	335,429	6,610.4	5,074	7.2	14.3
Brisbane – Inner City	298,121	8,173.9	3,647	8.6	14.4
Adelaide – West	247,123	15,953.9	1,549	10.2	24.4

Source: Australian Bureau of Statistics, 2021

During the summer of 2023, the highest maximum daily temperature was recorded in Adelaide, while Sydney experienced the lowest maximum daily temperature (*Table 3*). The mean temperature across the four study zones ranged from 26.1°C to 30.0°C, with Brisbane recording the highest mean temperature, while Melbourne was the lowest (*Table 3*).

Table 3: Temperature data for each study area in January 2023

SA4 (Study area)	Weather station	Maximum daily (°C)	Minimum daily (°C)	Monthly mean (°C)
Melbourne – Inner	Melbourne Olympic park	37.6	18.7	26.1
Sydney – City and Inner South	Sydney Airport	33.3	20.0	26.6
Brisbane – Inner City	Brisbane	34.4	26.4	30.0
Adelaide – West	Adelaide Airport	40.4	21.6	29.1

Source: Bureau of Meteorology, 2023

LST and land cover indices were calculated using USGS Landsat 8 Level 2, Collection 2, Tier 2 data catalogue. The data catalogue was filtered based on the study areas and the time period of focus, which is the summer of 2023 (1st of December 2022 to 28th of February 2023). The median of the images that fall within this time period was computed to obtain the satellite image for each city, as shown in *Figure 2*. These satellite images were used to calculate LST and land cover indices. This dataset is suitable for studying LST and land cover for several reasons. The Landsat-8 satellite captures data at 16-day intervals, providing ample data for the duration of the study. The sensors of the satellite also have a spatial resolution of 30 metres for visible, near-infrared (NIR), and short-wave infrared (SWIR), and 100 metres for thermal bands (resampled to 30 metres to match other bands). These resolutions are adequate for capturing urban features. The dataset also offers multi-spectral bands, allowing for the calculation of various remote sensing indices. Lastly, creating median composites helps mitigate the effect of cloud cover and makes the dataset more robust to outliers.

Figure 2: Median composites of satellite imagery representing Melbourne (A), Sydney (B), Brisbane (C), and Adelaide (D). Each image depicts the SA4 selected for each capital city.

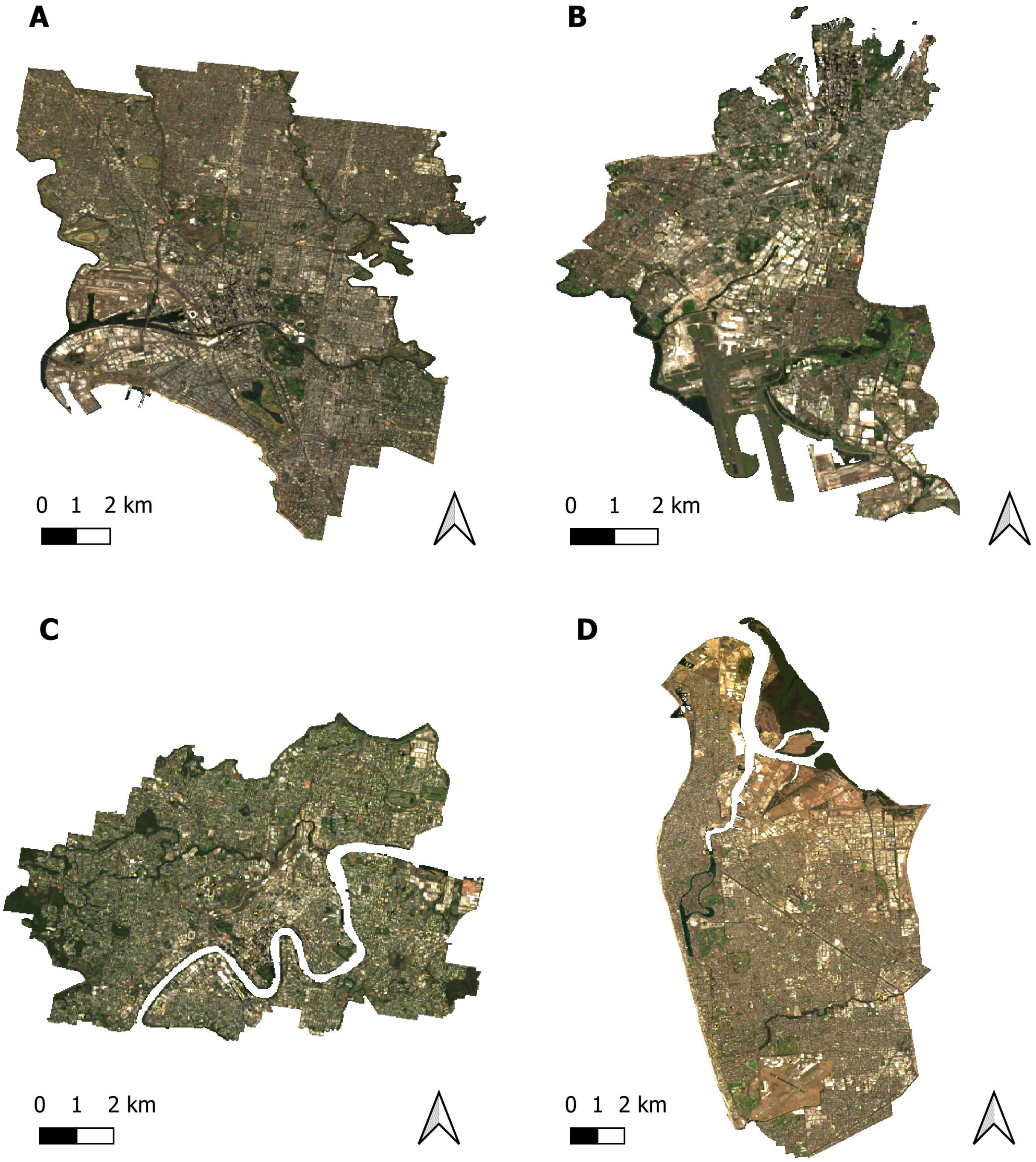

Source: USGS Landsat 8 Level 2, Collection 2, Tier 2

2.2. Calculation of LST and Land Cover Indices

Google Earth Engine (GEE) was used for all GIS data processing tasks and calculation of indices. Landsat-8 Thermal Infrared Sensor captures temperature data in thermal bands, which can be used to calculate LST. The LST was calculated using a series of equations described by Asad et al. (2023). First, we calculated the Normalized Difference Vegetation Index (NDVI) using *Equation 1*:

$$NDVI = \frac{Red - NIR}{Red + NIR} \tag{1}$$

where *Red* is the red band, and *NIR* represents the Near-Infrared band. The NDVI was then used to calculate fractional vegetation (*Pv*) using *Equation 2*:

$$Pv = [\frac{NDVI - NDVI_s}{NDVI_V - NDVI_s}]^2 \tag{2}$$

where $NDVI_s$ is the minimum NDVI and $NDVI_V$ is the maximum NDVI. The fractional vegetation allowed us to determine the land surface emissivity (ε) using *Equation 3* (Sobrino et al., 2004):

$$\varepsilon = 0.004Pv + 0.986 \tag{3}$$

Finally, we computed the LST of each pixel using *Equation 4* (Asad et al., 2023):

$$LST = \frac{Tb}{1 + \left(0.00115 \times \frac{Tb}{1.438}\right) \times \log(\varepsilon)} - 273.15 \tag{4}$$

where *Tb* is the Landsat 8 thermal band. For the calculation of EVI, BU, and MNDWI, we used data from Landsat-8's Operational Land Imager, which captures visible, NIR, and SWIR wavelengths. The EVI was calculated using *Equation 5*:

$$EVI = 2.5 \times \frac{NIR - Red}{NIR + (C_1 \times Red - C_2 \times Blue) + L} \tag{5}$$

where *NIR* is the near-infrared band, *Red* is the red band, and *Blue* is the blue band. *L* is the soil-adjustment factor, C_1 and C_2 are coefficients for correcting atmospheric scattering (Matsushita et al., 2007). Generally, *L*, C_1, and C_2 are assigned the values of 1, 6, and 7.5, respectively (Huete et al., 1997). This index has been found to significantly reduce noise caused by complex soil and atmosphere conditions compared to NDVI (Liu & Huete, 1995).

NDVI and NDBI are needed to calculate BU and can be computed using *Equation 1* and *Equation 6*, respectively:

$$NDBI = \frac{SWIR - NIR}{SWIR + NIR} \tag{6}$$

Where *SWIR* is the short-wave infrared band and *NIR* is the near-infrared band. BU is the improved version of NDBI as it distinguishes built-up areas from bare land by subtracting NDVI from NDBI (He et al., 2010).

MNDWI is a modified formula from NDWI, which suppresses the noise from built-up features, making it a better index for quantifying water surfaces in urban environments (Ali et al., 2019). It can be calculated using *Equation 7* (Xu, 2005):

$$NDWI = \frac{Green - SWIR}{Green + SWIR} \tag{7}$$

where *Green* represents the green band and *SWIR* represents the short-wave infrared band.

A water mask was generated using the permanent water layer dataset provided by the European Commission's Joint Research Centre (JRC) and applied to EVI and BU. This was done to eliminate noise caused by water bodies since they exhibit low LST and can represent exceptionally low EVI or very high BU. Such interference could potentially introduce inaccuracies in correlation analysis, making the results less representative of the actual vegetation or built-up land cover.

2.3. Correlation Analysis

The computed LST and three land cover indices were combined to form a single GEE Image. Approximately 1,000 points containing LST and land cover indices data were sampled from the GEE Image of each city. We then utilized R Programming Language to perform correlation analysis by creating a linear regression model and computing the R^2 value to illustrate the relationship between LST and each of the three land cover indices. We then calculated the Pearson's correlation coefficient for each pair of variables to analyze the strength and direction of the association between variables, as well as the significance of the coefficient by setting the significance level (alpha) at 0.01. The overall workflow for each study area is presented in *Figure 3*.

Figure 3: Workflow diagram describing the geoprocessing and correlation analysis processes for each study area

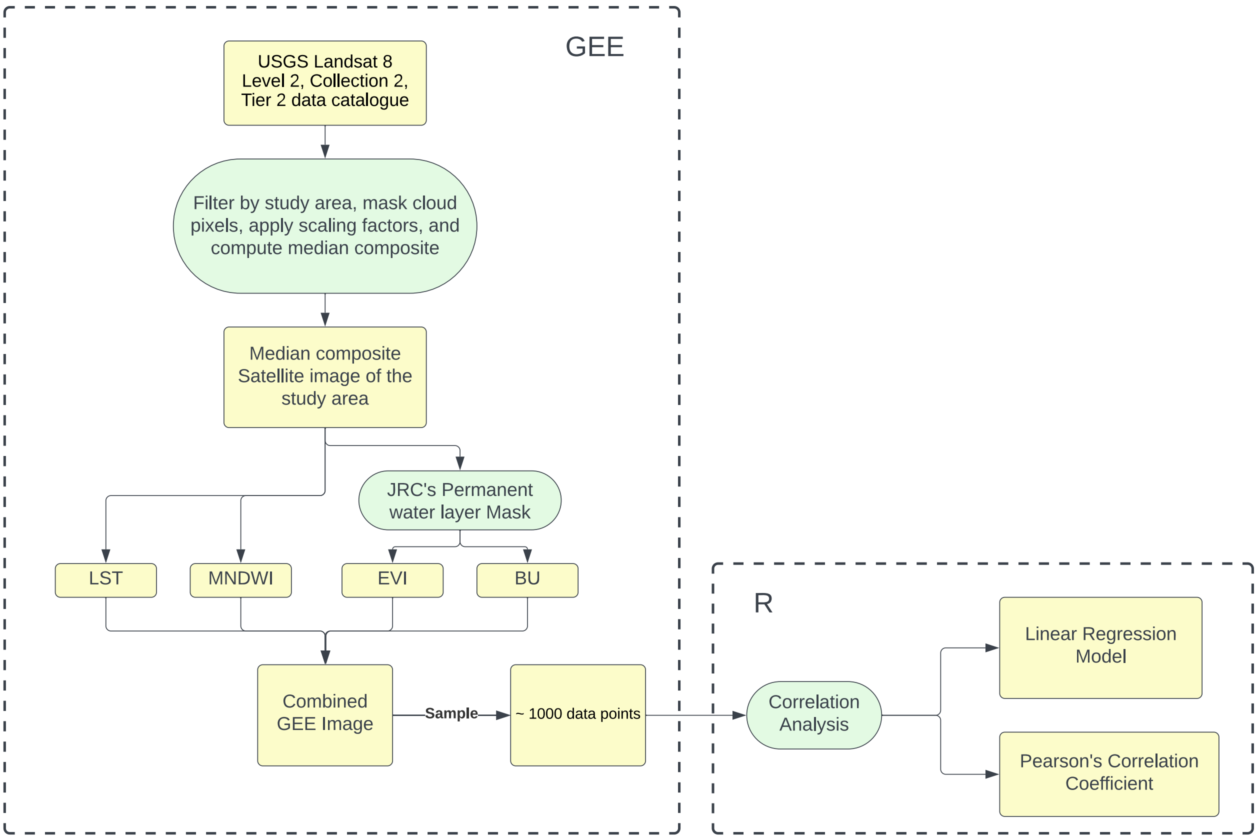

3. Results

3.1. Spatial Pattern of LST and Land Cover Indices

Upon visual analysis, areas with high EVI generally had lower LST, and areas with high BU mostly had higher LST across the four study areas (*Figure 4*). Water bodies (MNDWI greater than 0.5) exhibited the lowest LST; however, land surfaces with low MNDWI had lower LST, suggesting that the MNDWI on land surfaces have an opposite relationship with LST to MNDWI of actual water bodies. Interestingly, the MNDWI on land surfaces also appeared to be correlated with EVI, where areas with high EVI exhibited lower MNDWI. All land cover indices, particularly BU, showed some degree of relationship with LST across the study areas, but none of the land cover indices had perfect association with LST. The northern area of Sydney with high BU highlights the imperfect relationship between BU and LST as low LST was derived in this area.

Figure 4: Spatial pattern of LST, EVI, BU, and MNDWI for Melbourne (A - D), Sydney (E - H), Brisbane (I - L), and Adelaide (M - P) in the summer of 2023

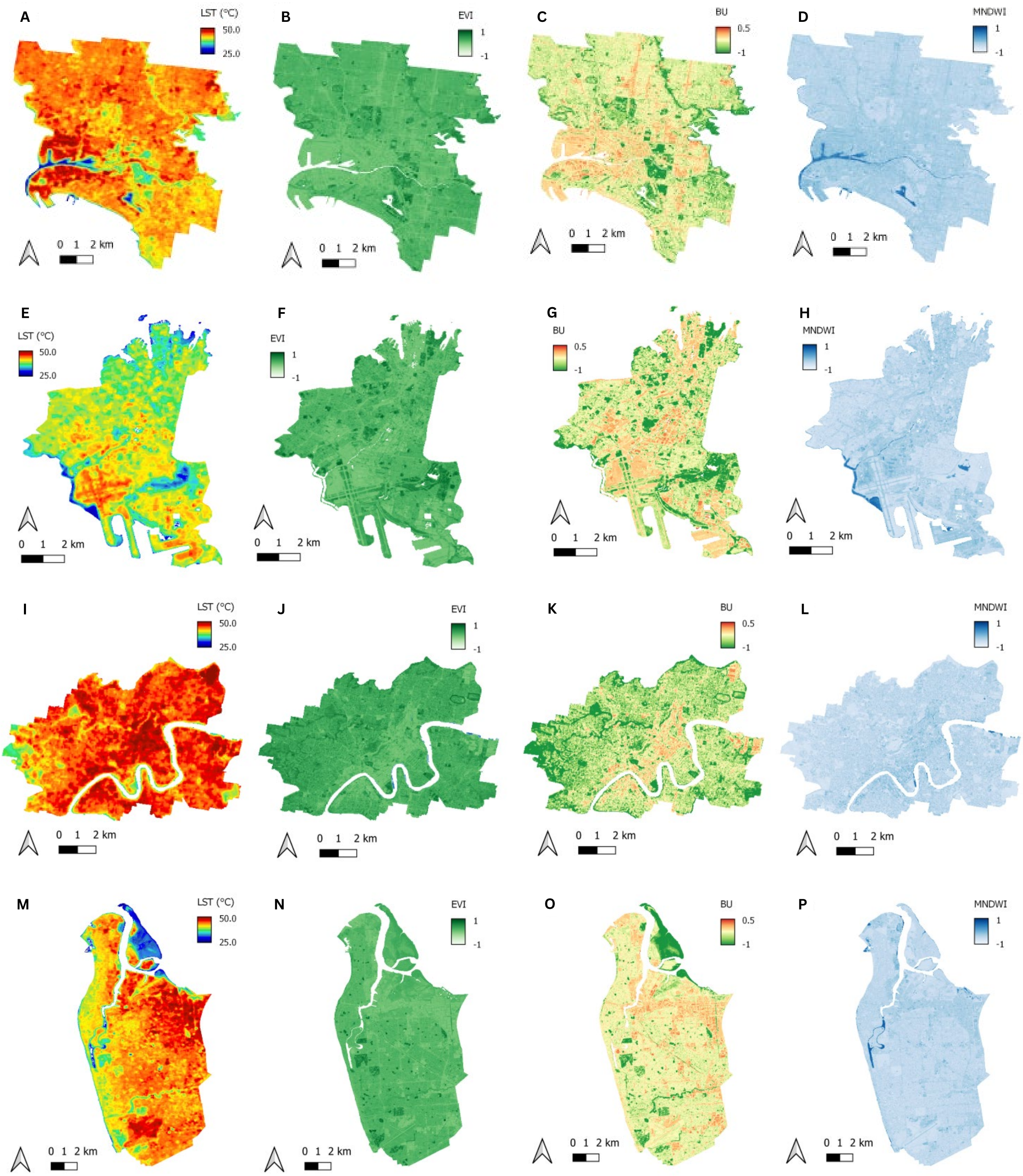

Source: USGS Landsat 8 Level 2, Collection 2, Tier 2

3.2. Correlation Analysis

The relationships between LST and land cover indices were consistent for all four cities, except the relationship between LST and MNDWI (*Figure 5*). Specifically, LST demonstrated a positive relationship with BU but a negative relationship with both EVI. The relationship with MNDWI was positive for Sydney and Brisbane but negative for Melbourne and Adelaide. However, the R-squared values were low for all land cover indices across the study sites, each falling below 0.6. Notably, MNDWI exhibited the weakest relationship with LST as shown by its relatively lower R-squared values (0.002 – 0.05), while BU displayed the strongest, as reflected in their relatively higher R-squared values (0.34 – 0.55). From the observed LST at the sampled points, Brisbane had the highest LST values, while Adelaide had the lowest temperatures.

Figure 5: Linear regression model of the relationship between LST and land cover indices computed using the sampled points from each city. *n* represents the number of sample points used (*n* was higher for MNDWI due to the absence of permanent water mask.)

Melbourne (n = 964 for EVI and BU, n = 1023 for MNDWI)

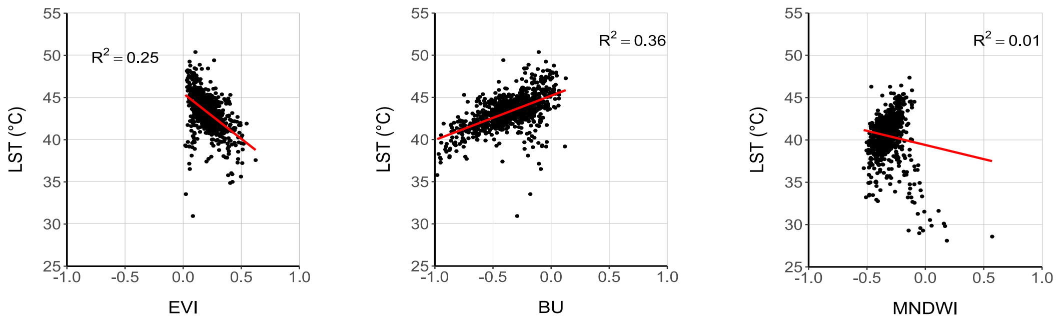

Sydney (n = 965 for EVI and BU, n = 1075 for MNDWI)

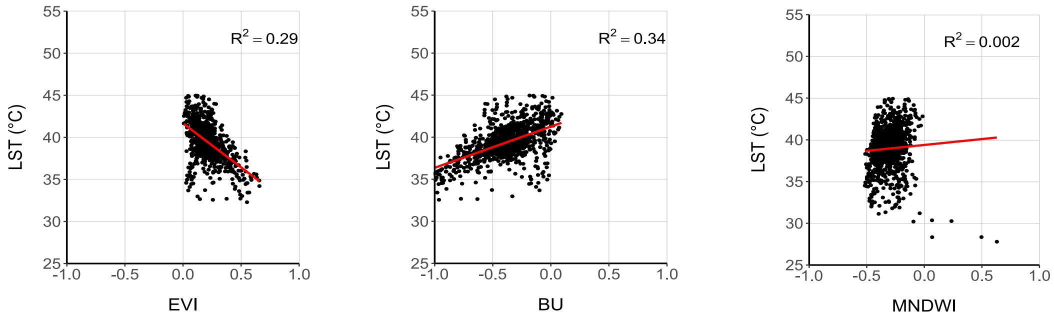

Brisbane (n = 1045 for EVI and BU, n = 1089 for MNDWI)

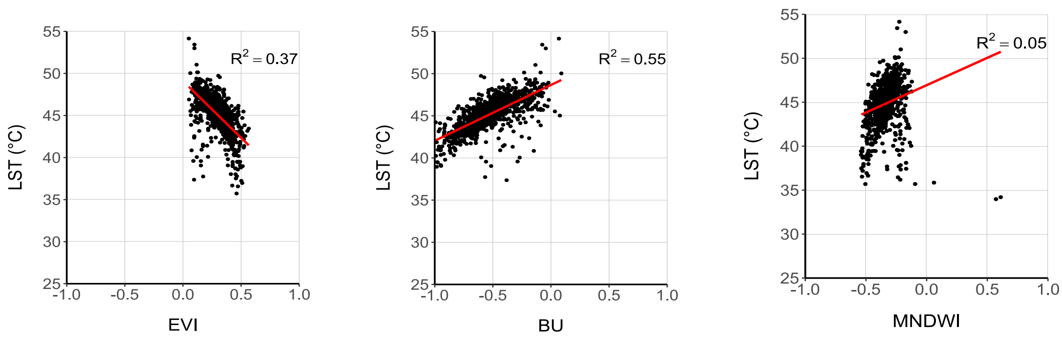

Adelaide (n = 1047 for EVI and BU, n = 1108 for MNDWI)

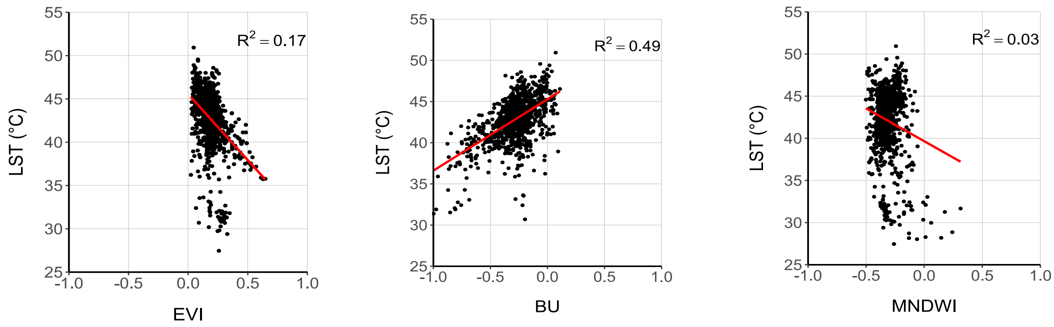

The Pearson correlation coefficients presented in *Table 4* consistently align with the findings of the linear regression model (*Figure 5*), as shown by the negative correlation coefficients for LST - EVI and the positive correlation coefficients for LST - BU. The Pearson correlation coefficients of LST - MNDWI were positive for Brisbane and Sydney, but negative for Melbourne and Adelaide. Importantly, the relationships between LST and every land cover index of all cities were found to be statistically significant at a significance level of 0.01, except LST – MNDWI for Sydney. The strength of the correlation varied among the land cover indices, with BU showing the strongest correlation, followed by EVI, and then MNDWI; this order was consistent across the four cities.

When comparing these correlation coefficients between cities, Brisbane had the strongest relationship between LST and land cover indices (*Table 4*). Melbourne and Sydney displayed relatively weaker correlation compared to Brisbane, and the correlation strength of Melbourne and Sydney were at very similar levels for all three land cover indices. Adelaide showed the weakest relationship for all three land cover indices; however, Adelaide's BU and EVI were not significantly distant from those observed in Melbourne and Sydney.

Table 4: Pearson correlation coefficients for LST and land cover indices in major Australian cities

City	LST - EVI	LST - BU	LST - MNDWI
Melbourne	- 0.54*	0.63*	-0.13*
Sydney	- 0.54*	0.58*	0.06
Brisbane	- 0.61*	0.75*	0.23*
Adelaide	- 0.41*	0.70*	-0.18*

* Correlation is significant at the 0.01 level

4. Discussion

Our findings suggest that LST had a robust positive correlation with built-up features and a negative relationship with vegetation. Most correlation pairs were statistically significant, ruling out the likelihood of relationship being due to random chance. Prior studies using similar indices observed the same relationship with vegetation indices and built-up indices (Das et al., 2021; Q. Sun et al., 2012). The results also show the difference in correlation strength among land cover indices, where BU exhibited the strongest correlation, a pattern that was consistent throughout the four cities. This aligns with previous studies, which have shown that NDBI, a similar land cover index for built-up features, demonstrates stronger correlations with LST than a vegetation index such as NDVI (Chen et al., 2013; Guha et al., 2018). This suggests that urban development and construction activities have a more significant impact on local temperatures; therefore, regulating built-up areas is an effective strategy for mitigating UHI (Yin et al., 2018). However, regulating urban development may not always be ideal as urban areas may need to expand in order to support the growing population and economy. Although the correlation strength with vegetation is weaker, we found that EVI was negatively correlated with LST; therefore, sustainable urban designs with enhanced green spaces could be a more feasible strategy for Australian cities (Aflaki et al., 2017).

MNDWI, however, was found to be negatively correlated with LST in past studies, unlike our findings for Brisbane and Sydney, which exhibited a positive relationship (Das et al., 2021; Guha &

Govil, 2022; Q. Sun et al., 2012). This highlights a limitation in using MNDWI since it can be misleading for land surfaces. *Figure 4* shows that land areas with low MNDWI were typically associated with high EVI, which tended to have low LST, so the MNDWI was likely to be positively correlated with LST. The satellite imagery was clipped using polygon data from ABS, which mostly excluded water bodies; therefore, most sample points were based on land and insufficient sample points were collected on water bodies to show the true relationship between LST and water bodies. This is evident in *Figure 5* where most sample points of MNDWI for all cities were on the negative side. However, MNDWI was still useful for identifying water bodies with positive MNDWI values, confirming that the lowest LST could be observed at water bodies, as observed in *Figures 4* and *5*. This implies that urban water bodies, such as rivers and wetlands, can play a significant role in mitigating UHI in nearby areas (Murakawa et al., 1991).

Another limitation of this study is that EVI and BU were highly correlated, as seen in *Figure 4*, due to the use of the same bands in the calculation of both indices, namely red and near-infrared bands. This led to the problem of multicollinearity, which reduces the regression model's reliability and interpretability. Specifically, multicollinearity between EVI and BU made it unclear whether the variations in LST in the analysis using BU were due to the level of vegetation cover or the intensity of built-up area (NDVI was used in the calculation of BU). Therefore, it is hard to conclude that built-up area was solely the cause of high LST if multicollinearity existed. Furthermore, using only three land cover indices simplifies the complexity of land cover and may not represent the full diversity of land cover types and conditions in the study areas; therefore, the analysis could not fully explain the underlying processes of the variations in LST. Including more indices and variables, such as NDBaI and elevation, could provide a more comprehensive understanding of spatial variation in LST (Alexander, 2020; Q. Sun et al., 2012).

In conclusion, our findings revealed significant correlations between LST and land cover indices, where increasing built-up areas leads to an increase in LST and increasing urban vegetation results in a decrease in LST. These results have implications for urban planning as they highlight the need to manage urban development and enhance urban vegetation to mitigate UHI effects in Australian cities. Future research should extensively investigate urban LST using a wider array of independent indices to enhance the reliability of regression models and gain a more comprehensive understanding of the spatial variations in LST within urban environments.

Word Count: 3,141 (Includes everything except table values, references, and appendix)

5. Reference

Aflaki, A., Mirnezhad, M., Ghaffarianhoseini, A., Ghaffarianhoseini, A., Omrany, H., Wang, Z.-H., & Akbari, H. (2017). Urban heat island mitigation strategies: A state-of-the-art review on Kuala Lumpur, Singapore and Hong Kong. *Cities*, *62*, 131-145.

Ahmed, B., Kamruzzaman, M., Zhu, X., Rahman, M. S., & Choi, K. (2013). Simulating Land Cover Changes and Their Impacts on Land Surface Temperature in Dhaka, Bangladesh. *Remote Sensing*, *5*(11), 5969-5998. https://www.mdpi.com/2072-4292/5/11/5969

Alexander, C. (2020). Normalised difference spectral indices and urban land cover as indicators of land surface temperature (LST). *International Journal of Applied Earth Observation and Geoinformation*, *86*, 102013.

Ali, M. I., Dirawan, G. D., Hasim, A. H., & Abidin, M. R. (2019). Detection of changes in surface water bodies urban area with NDWI and MNDWI methods. *International Journal on Advanced Science Engineering Information Technology*, *9*(3), 946-951.

Asad, A., Ullah, K., Butt, M. J., & Labban, A. b. H. (2023). Analysis of urban heat island effects in high altitude areas of Pakistan. *Remote Sensing Applications: Society and Environment*, *32*, 101071. https://doi.org/https://doi.org/10.1016/j.rsase.2023.101071

Australian Bureau of Statistics. (2014). 3218.0 - Regional population growth, Australia, 2012–13: Feature Article: Capital Cities: Past, Present and Future. http://www.abs.gov.au/ausstats/abs@.nsf/Previousproducts/3218.0Feature%20Article22012-13?opendocument&tabname=Summary&prodno=3218.0&issue=2012-13&num=&view=

Chen, L., Li, M., Huang, F., & Xu, S. (2013, 16-18 Dec. 2013). Relationships of LST to NDBI and NDVI in Wuhan City based on Landsat ETM+ image. 2013 6th International Congress on Image and Signal Processing (CISP),

Das, N., Mondal, P., Sutradhar, S., & Ghosh, R. (2021). Assessment of variation of land use/land cover and its impact on land surface temperature of Asansol subdivision. *The Egyptian Journal of Remote Sensing and Space Science*, *24*(1), 131-149. https://doi.org/https://doi.org/10.1016/j.ejrs.2020.05.001

Guha, S., & Govil, H. (2022). Annual assessment on the relationship between land surface temperature and six remote sensing indices using landsat data from 1988 to 2019. *Geocarto International*, *37*(15), 4292-4311. https://doi.org/10.1080/10106049.2021.1886339

Guha, S., Govil, H., Dey, A., & Gill, N. (2018). Analytical study of land surface temperature with NDVI and NDBI using Landsat 8 OLI and TIRS data in Florence and Naples city, Italy. *European Journal of Remote Sensing*, *51*(1), 667-678. https://doi.org/10.1080/22797254.2018.1474494

Gunawardena, K. R., Wells, M. J., & Kershaw, T. (2017). Utilising green and bluespace to mitigate urban heat island intensity. *Science of The Total Environment*, *584*, 1040-1055.

He, C., Shi, P., Xie, D., & Zhao, Y. (2010). Improving the normalized difference built-up index to map urban built-up areas using a semiautomatic segmentation approach. *Remote Sensing Letters*, *1*(4), 213-221.

Huete, A. R., Liu, H. Q., Batchily, K., & van Leeuwen, W. (1997). A comparison of vegetation indices over a global set of TM images for EOS-MODIS. *Remote sensing of Environment*, *59*(3), 440-451. https://doi.org/https://doi.org/10.1016/S0034-4257(96)00112-5

Li, X., Zhou, Y., Yu, S., Jia, G., Li, H., & Li, W. (2019). Urban heat island impacts on building energy consumption: A review of approaches and findings. *Energy*, *174*, 407-419. https://doi.org/https://doi.org/10.1016/j.energy.2019.02.183

Liu, H. Q., & Huete, A. (1995). A feedback based modification of the NDVI to minimize canopy background and atmospheric noise. *IEEE Transactions on Geoscience and Remote Sensing*, *33*(2), 457-465. https://doi.org/10.1109/TGRS.1995.8746027

Matsushita, B., Yang, W., Chen, J., Onda, Y., & Qiu, G. (2007). Sensitivity of the Enhanced Vegetation Index (EVI) and Normalized Difference Vegetation Index (NDVI) to Topographic Effects: A Case Study in High-density Cypress Forest. *Sensors*, *7*(11), 2636-2651. https://www.mdpi.com/1424-8220/7/11/2636

Murakawa, S., Sekine, T., Narita, K.-i., & Nishina, D. (1991). Study of the effects of a river on the thermal environment in an urban area. *Energy and Buildings*, *16*(3-4), 993-1001.

Nuruzzaman, M. (2015). Urban heat island: causes, effects and mitigation measures-a review. *International Journal of Environmental Monitoring and Analysis*, *3*(2), 67-73.

Parker, D. E. (2010). Urban heat island effects on estimates of observed climate change. *Wiley Interdisciplinary Reviews: Climate Change*, *1*(1), 123-133.

Rizwan, A. M., Dennis, L. Y. C., & Liu, C. (2008). A review on the generation, determination and mitigation of Urban Heat Island. *Journal of Environmental Sciences*, *20*(1), 120-128. https://doi.org/https://doi.org/10.1016/S1001-0742(08)60019-4

Rogers, C. D. W., Gallant, A. J. E., & Tapper, N. J. (2019). Is the urban heat island exacerbated during heatwaves in southern Australian cities? *Theoretical and Applied Climatology*, *137*(1), 441-457. https://doi.org/10.1007/s00704-018-2599-x

Santamouris, M. (2015). Analyzing the heat island magnitude and characteristics in one hundred Asian and Australian cities and regions. *Science of The Total Environment*, *512-513*, 582-598. https://doi.org/https://doi.org/10.1016/j.scitotenv.2015.01.060

Sharma, R., Hooyberghs, H., Lauwaet, D., & De Ridder, K. (2019). Urban Heat Island and Future Climate Change—Implications for Delhi's Heat. *Journal of Urban Health*, *96*(2), 235-251. https://doi.org/10.1007/s11524-018-0322-y

Sun, Q., Wu, Z., & Tan, J. (2012). The relationship between land surface temperature and land use/land cover in Guangzhou, China. *Environmental Earth Sciences*, *65*(6), 1687-1694. https://doi.org/10.1007/s12665-011-1145-2

Sun, R., Chen, A., Chen, L., & Lü, Y. (2012). Cooling effects of wetlands in an urban region: The case of Beijing. *Ecological Indicators*, *20*, 57-64. https://doi.org/https://doi.org/10.1016/j.ecolind.2012.02.006

Xu, H. (2005). A study on information extraction of water body with the modified normalized difference water index (MNDWI). *JOURNAL OF REMOTE SENSING-BEIJING-*, *9*(5), 595.

Yang, L., Qian, F., Song, D.-X., & Zheng, K.-J. (2016). Research on Urban Heat-Island Effect. *Procedia Engineering*, *169*, 11-18. https://doi.org/https://doi.org/10.1016/j.proeng.2016.10.002

Yin, C., Yuan, M., Lu, Y., Huang, Y., & Liu, Y. (2018). Effects of urban form on the urban heat island effect based on spatial regression model. *Science of The Total Environment*, *634*, 696-704. https://doi.org/https://doi.org/10.1016/j.scitotenv.2018.03.350

Yin, Z., Liu, Z., Liu, X., Zheng, W., & Yin, L. (2023). Urban heat islands and their effects on thermal comfort in the US: New York and New Jersey. *Ecological Indicators*, *154*, 110765. https://doi.org/https://doi.org/10.1016/j.ecolind.2023.110765

6. Appendix (Google Earth Engine Code)

Link - https://code.earthengine.google.com/3cfd9047d5ffcea4e9cfb782f7894854

```
/*
Relationship between LST and Land Cover Indices
Author: Warin Chotirosniramit
Date: 2023-10-24

*/


// Function to mask clouds based on the pixel_qa band of Landsat data.
function cloudMaskFunc(image) {
  // Bits 3 and 5 are cloud shadow and cloud, respectively.
  var cloudShadowBitMask = (1 << 4);
  var cloudsBitMask = (1 << 3);
  // Get the pixel QA band, which contains information about various pixel
properties,
  // including cloud and cloud shadow information.
  var qa = image.select('QA_PIXEL');
  // Both flags should be set to zero, indicating clear conditions.
  var mask = qa.bitwiseAnd(cloudShadowBitMask).eq(0)
                .and(qa.bitwiseAnd(cloudsBitMask).eq(0));
  return image.updateMask(mask);
}


// Applies scaling factors.
function applyScaleFactors(image) {
  var opticalBands = image.select('SR_B.').multiply(0.0000275).add(-0.2);
  var thermalBands = image.select('ST_B.*').multiply(0.00341802).add(149.0);
  return image.addBands(opticalBands, null, true)
              .addBands(thermalBands, null, true);
}


var waterOcc = ee.Image("JRC/GSW1_4/GlobalSurfaceWater").select('occurrence'),
    jrc_data0 = ee.Image("JRC/GSW1_0/Metadata").select('total_obs').lte(0),
    waterOccFilled = waterOcc.unmask(0).max(jrc_data0),
    waterMask = waterOccFilled.lt(50);

// Create visualization parameters
var vizParams = {
  bands: ['SR_B4','SR_B3','SR_B2'],
  min:0,
  max: 0.3,
};

var LST_viz = {min: 20, max:50, palette:[
  '040274','040281','0502a3','0502b8','0502ce','0502e6',
  '0602ff','235cb1','307ef3','269db1','30c8e2','32d3ef',
  '3be285','3ff38f','86e26f','3ae237','b5e22e','d6e21f',
  'fff705','ffd611','ffb613','ff8b13','ff6e08','ff500d',
  'ff0000','de0101','c21301','a71001','911003']};
```

```
var eviParams = {min: -1, max: 1, palette: ['blue', 'white', 'green']};

var buParams = {min: -1, max: 1, palette: ['1a9641', 'a6d96a', 'ffffc0',
'fdae61','d7191c']};

var mndwiParams = {min: -1, max:1,palette: ['#f7fbff', '#deebf7', '#c6dbef',
'#9ecae1', '#6baed6', '#4292c6', '#2171b5', '#08519c', '#08306b']};

// var mbiParams = {min: -0.5, max: 1.5, palette:['#018571', '#80cdc1',
'#f5f5f5', '#dfc27d', '#a6611a']};

// Define a function to compute Land Surface Temperature (LST)
function computeLST(image, city) {
  // NDVI
  var ndvi = image.normalizedDifference(['SR_B5', 'SR_B4']).rename('NDVI');
  var ndviParams = { min: -1, max: 1, palette: ['blue', 'white', 'green'] };

  // min and max of NDVI
  var min = ee.Number(ndvi.reduceRegion({
    reducer: ee.Reducer.min(),
    scale: 30,
    maxPixels: 1e9
  }).values().get(0));

  var max = ee.Number(ndvi.reduceRegion({
    reducer: ee.Reducer.max(),
    scale: 30,
    maxPixels: 1e9
  }).values().get(0));

  // Fractional vegetation
  var fv =
(ndvi.subtract(min).divide(max.subtract(min))).pow(ee.Number(2)).rename('Fractio
nalVegetation');
  var imageVisParam3 = { min: 0.9865619146722164, max: 0.989699971371314 };

  // Emissivity
  var a = ee.Number(0.004);
  var b = ee.Number(0.986);
  var EM = fv.multiply(a).add(b).rename('EMM');

  // Landsat Band10: Brightness Temperature
  var thermal = image.select('ST_B10').multiply(0.1);

  // Land surface temperature
  var LST = thermal.expression(
  '(Tb/(1 + (0.00115* (Tb/1.438))*log(Ep)))-273.15',
  {'Tb': image.select('ST_B10'),
  'Ep': EM.select('EMM')}).rename('LST');

  Map.addLayer(LST, LST_viz, city + ' LST');

  Export.image.toDrive({
  image: LST.copyProperties(image, image.propertyNames()),
  description: city+ '_LST',
  folder: 'GEOG3301 GEE Products',
  scale: 30,
  maxPixels: 1e10,
});
```

```
  return LST;

}

// Define EVI function

function computeEVI(image, city) {
  var evi = image.expression(
  '2.5 * ((B5 - B4) / (B5 + 6 * B4 - 7.5 * B2 + 1))', {
    'B5': image.select('SR_B5'), // Near-Infrared (Band 5)
    'B4': image.select('SR_B4'), // Red (Band 4)
    'B2': image.select('SR_B2')  // Blue (Band 2)
  }).rename('EVI').updateMask(waterMask);

  Map.addLayer(evi, eviParams, city + ' EVI');

  Export.image.toDrive({
  image: evi.copyProperties(image, image.propertyNames()),
  description: city+ '_EVI',
  folder: 'GEOG3301 GEE Products',
  scale: 30,
  maxPixels: 1e10,
});

  return evi;
}

// Define BU function

function computeBU(image, city) {
  var ndbi = image.normalizedDifference(['SR_B6', 'SR_B5']).rename('NDBI');
  var ndvi = image.normalizedDifference(['SR_B5', 'SR_B4']).rename('NDVI');
  var bu = ndbi.subtract(ndvi).rename('BU').updateMask(waterMask);

  Map.addLayer(bu, buParams, city+ ' BU');

  Export.image.toDrive({
  image: bu.copyProperties(image, image.propertyNames()),
  description: city+ '_BU',
  folder: 'GEOG3301 GEE Products',
  scale: 30,
  maxPixels: 1e10,
});

  return bu;
}

// Define MNDWI function

function computeMNDWI(image, city) {
  var mndwi = image.normalizedDifference(['SR_B3', 'SR_B6']).rename('MNDWI');
  Map.addLayer(mndwi, mndwiParams, city + ' MNDWI');

  Export.image.toDrive({
  image: mndwi,
  description: city+ '_MNDWI',
  folder: 'GEOG3301 GEE Products',
  scale: 30,
```

```
  maxPixels: 1e10,
});

  return mndwi;
}


// -------------- Melbourne --------------

// Load the shapefile of Melbourne
var Melbourne = ee.FeatureCollection(Melbourne).geometry();

// load the collection:
{
var col = ee.ImageCollection('LANDSAT/LC08/C02/T1_L2')
.map(cloudMaskFunc)
.map(applyScaleFactors)
.filterBounds(Melbourne)
.filterMetadata('CLOUD_COVER_LAND', 'less_than', 1)
.filterDate('2022-12-01','2023-02-28')}

// Melbourne Satellite image
{
var Melb_sat = col.median().clip(Melbourne);
Map.addLayer(Melb_sat, vizParams, 'Melbourne');
}

Export.image.toDrive({
  image: Melb_sat,
  description: "Melb_sat",
  folder: 'GEOG3301 GEE Products',
  scale: 30,
  maxPixels: 1e10,
});

// Melbourne LST and LC indices

var Melb_LST = computeLST(Melb_sat, 'Melbourne');

var Melb_EVI = computeEVI(Melb_sat, 'Melbourne');

var Melb_BU = computeBU(Melb_sat, 'Melbourne');

var Melb_MNDWI = computeMNDWI(Melb_sat, 'Melbourne');

// var Melb_MBI = computeMBI(Melb_sat, 'Melbourne');


// Create a feature collection of all bands and sample points
var Melb_LST_indices = Melb_LST.addBands(Melb_EVI).addBands(Melb_BU).sample({
  region: Melbourne, // Define your region of interest
  scale: 420, // Adjust the scale as needed
});

print(Melb_LST_indices, 'Melbourne LST and LC indices');

// Export the feature collection to Google Drive or another destination
Export.table.toDrive({
  collection: Melb_LST_indices,
```

```
  folder: 'GEOG3301 GEE Products',
  description: 'Melbourne_Table', // Specify the table's name
  fileFormat: 'CSV' // Export as CSV or other desired format
});


// Create a feature collection of all bands and sample points for MNDWI
var Melb_LST_indices_MNDWI = Melb_LST.addBands(Melb_MNDWI).sample({
  region: Melbourne, // Define your region of interest
  scale: 420, // Adjust the scale as needed
});

print(Melb_LST_indices_MNDWI, 'Melbourne LST and LC indices');

// Export the feature collection to Google Drive or another destination
Export.table.toDrive({
  collection: Melb_LST_indices_MNDWI,
  folder: 'GEOG3301 GEE Products',
  description: 'Melbourne_Table_MNDWI', // Specify the table's name
  fileFormat: 'CSV' // Export as CSV or other desired format
});

// --------------- Sydney ----------------

// Load the shapefile of Sydney
var Sydney = ee.FeatureCollection(Sydney).geometry();

// load the collection:
{
var syd_col = ee.ImageCollection('LANDSAT/LC08/C02/T1_L2')
.map(cloudMaskFunc)
.map(applyScaleFactors)
.filterBounds(Sydney)
.filterMetadata('CLOUD_COVER_LAND', 'less_than', 1)
.filterDate('2022-12-01','2023-02-28')}

// Sydney Satellite image on 2023-02-02
{
var Syd_sat = syd_col.median().clip(Sydney);
Map.addLayer(Syd_sat, vizParams, 'Sydney');
}

Export.image.toDrive({
  image: Syd_sat,
  description: "Syd_sat",
  folder: 'GEOG3301 GEE Products',
  scale: 30,
  maxPixels: 1e10,
});

// Sydney LST and LC indices

var Syd_LST = computeLST(Syd_sat, 'Sydney');

var Syd_EVI = computeEVI(Syd_sat, 'Sydney');

var Syd_BU = computeBU(Syd_sat, 'Sydney');

var Syd_MNDWI = computeMNDWI(Syd_sat, 'Sydney');
```

```
// Create a feature collection of all bands and sample points
var Syd_LST_indices =
Syd_LST.addBands(Syd_EVI).addBands(Syd_BU).addBands(Syd_MNDWI).sample({
  region: Sydney, // Define your region of interest
  scale: 270, // Adjust the scale as needed
});

print(Syd_LST_indices, 'Sydney LST and LC indices');

// Export the feature collection to Google Drive or another destination
Export.table.toDrive({
  collection: Syd_LST_indices,
  folder: 'GEOG3301 GEE Products',
  description: 'Sydney_Table', // Specify the table's name
  fileFormat: 'CSV' // Export as CSV or other desired format
});

// Create a feature collection of all bands and sample points for  MNDWI
var Syd_LST_indices_MNDWI = Syd_LST.addBands(Syd_MNDWI).sample({
  region: Sydney, // Define your region of interest
  scale: 270, // Adjust the scale as needed
});

print(Syd_LST_indices_MNDWI, 'Sydney LST and LC indices');

// Export the feature collection to Google Drive or another destination
Export.table.toDrive({
  collection: Syd_LST_indices_MNDWI,
  folder: 'GEOG3301 GEE Products',
  description: 'Sydney_Table_MNDWI', // Specify the table's name
  fileFormat: 'CSV' // Export as CSV or other desired format
});

// --------------- Brisbane ----------------

// Load the shapefile of Brisbane
var Brisbane = ee.FeatureCollection(Brisbane).geometry();

// load the collection:
{
var Bris_col = ee.ImageCollection('LANDSAT/LC08/C02/T1_L2')
.map(cloudMaskFunc)
.map(applyScaleFactors)
.filterBounds(Brisbane)
.filterMetadata('CLOUD_COVER_LAND', 'less_than', 30)
.filterDate('2022-12-01','2023-02-28')}

// Brisbane Satellite image on 2023-02-02
{
var Bris_sat = Bris_col.median().clip(Brisbane);
Map.addLayer(Bris_sat, vizParams, 'Brisbane');
}

Export.image.toDrive({
  image: Bris_sat,
  description: "Bris_sat",
  folder: 'GEOG3301 GEE Products',
  scale: 30,
```

```
  maxPixels: 1e10,
});

// Brisbane LST and LC indices

var Bris_LST = computeLST(Bris_sat, 'Brisbane');

var Bris_EVI = computeEVI(Bris_sat, 'Brisbane');

var Bris_BU = computeBU(Bris_sat, 'Brisbane');

var Bris_MNDWI = computeMNDWI(Bris_sat, 'Brisbane');

// Create a feature collection of all bands and sample points
var Bris_LST_indices = Bris_LST.addBands(Bris_EVI).addBands(Bris_BU).sample({
  region: Brisbane, // Define your region of interest
  scale: 290, // Adjust the scale as needed
});

print(Bris_LST_indices, 'Brisbane LST and LC indices');

// Export the feature collection to Google Drive or another destination
Export.table.toDrive({
  collection: Bris_LST_indices,
  folder: 'GEOG3301 GEE Products',
  description: 'Brisbane_Table', // Specify the table's name
  fileFormat: 'CSV' // Export as CSV or other desired format
});

// Create a feature collection of all bands and sample points for MNDWI
var Bris_LST_indices_MNDWI = Bris_LST.addBands(Bris_MNDWI).sample({
  region: Brisbane, // Define your region of interest
  scale: 290, // Adjust the scale as needed
});

print(Bris_LST_indices_MNDWI, 'Brisbane LST and LC indices');

// Export the feature collection to Google Drive or another destination
Export.table.toDrive({
  collection: Bris_LST_indices_MNDWI,
  folder: 'GEOG3301 GEE Products',
  description: 'Brisbane_Table_MNDWI', // Specify the table's name
  fileFormat: 'CSV' // Export as CSV or other desired format
});

// --------------- Adelaide ----------------

// Load the shapefile of Adelaide
var Adelaide = ee.FeatureCollection(Adelaide).geometry();

// load the collection:
{
var Ade_col = ee.ImageCollection('LANDSAT/LC08/C02/T1_L2')
.map(cloudMaskFunc)
.map(applyScaleFactors)
.filterBounds(Adelaide)
.filterMetadata('CLOUD_COVER_LAND', 'less_than', 30)
.filterDate('2022-12-01','2023-02-28')}
```

```
// Adelaide Satellite image on 2023-02-02
{
var Ade_sat = Ade_col.median().clip(Adelaide);
Map.addLayer(Ade_sat, vizParams, 'Adelaide');
}

Export.image.toDrive({
  image: Ade_sat,
  description: "Ade_sat",
  folder: 'GEOG3301 GEE Products',
  scale: 30,
  maxPixels: 1e10,
});

// Adelaide LST and LC indices

var Ade_LST = computeLST(Ade_sat, 'Adelaide');

var Ade_EVI = computeEVI(Ade_sat, 'Adelaide');

var Ade_BU = computeBU(Ade_sat, 'Adelaide');

var Ade_MNDWI = computeMNDWI(Ade_sat, 'Adelaide');

// Create a feature collection of all bands and sample points
var Ade_LST_indices =
Ade_LST.addBands(Ade_EVI).addBands(Ade_BU).addBands(Ade_MNDWI).sample({
  region: Adelaide, // Define your region of interest
  scale: 420, // Adjust the scale as needed
});

print(Ade_LST_indices, 'Adelaide LST and LC indices');

// Export the feature collection to Google Drive or another destination
Export.table.toDrive({
  collection: Ade_LST_indices,
  folder: 'GEOG3301 GEE Products',
  description: 'Adelaide_Table', // Specify the table's name
  fileFormat: 'CSV' // Export as CSV or other desired format
});

// Create a feature collection of all bands and sample points for MNDWI
var Ade_LST_indices_MNDWI = Ade_LST.addBands(Ade_MNDWI).sample({
  region: Adelaide, // Define your region of interest
  scale: 420, // Adjust the scale as needed
});

print(Ade_LST_indices_MNDWI, 'Adelaide LST and LC indices');

// Export the feature collection to Google Drive or another destination
Export.table.toDrive({
  collection: Ade_LST_indices_MNDWI,
  folder: 'GEOG3301 GEE Products',
  description: 'Adelaide_Table_MNDWI', // Specify the table's name
  fileFormat: 'CSV' // Export as CSV or other desired format
});
```